

1
2
3
4
5
6
7
8
9
10
11
12
13
14
15
16
17
18
19
20
21
22
23
24
25

UNIVERSITY OF CALIFORNIA
SANTA CRUZ

**AN INCLUSIVE SEARCH FOR THE DECAY OF A BOOSTED
HIGGS BOSON IN THE $H \rightarrow b\bar{b}$ CHANNEL WITH THE ATLAS
DETECTOR**

A dissertation submitted in partial satisfaction of the
requirements for the degree of
DOCTOR OF PHILOSOPHY

in

PARTICLE PHYSICS

by

Jacob Martin Pasner

October 2019

The Dissertation of Jacob Martin Pasner
is approved:

Professor Jason Nielsen, Chair

Professor Abraham Seiden

Professor Michael Hance

Dean Lori Kletzer
Vice Provost and Dean of Graduate Studies

Copyright © by

Jacob Martin Pasner

2019

31 **Table of Contents**

32	List of Figures	vii
33	List of Tables	x
34	Abstract	xi
35	Dedication	xii
36	Acknowledgments	xiii
37	1 Introduction	1
38	I Theoretical Motivations and the Standard Model	2
39	2 The Standard Model and Beyond	3
40	2.1 The Standard Model	4
41	2.1.1 Bosons	5
42	2.1.2 Fermions	8
43	2.2 Quantum Electrodynamics	8
44	2.3 Quantum Chromodynamics	12
45	2.4 The Higgs Mechanism	14

46	2.4.1	Electroweak Symmetry Breaking	14
47	2.4.2	Fermion Mass Terms	18
48	2.4.3	The Higgs Boson	18
49	II	Experimental Apparatus and Associated Facilities	19
50	3	The Large Hadron Collider	20
51	3.1	Particle Incjecton Chain	21
52	3.2	LHC layout and design	23
53	3.3	Performance	26
54	3.4	Pile-up at the LHC	28
55	4	The ATLAS Detector	30
56	4.1	ATLAS Coordinate System	33
57	4.2	Tracking with the Inner Detector	37
58	4.2.1	Pixel Detector	39
59	4.2.2	Semiconductor Tracker	39
60	4.2.3	Transition Radiation Tracker	40
61	4.3	Calorimetry	41
62	4.3.1	Electromagnetic Calorimeter	42
63	4.3.2	Hadronic Calorimeter	44
64	4.4	Muon Spectrometer	46
65	5	Boosted Higgs at the LHC	49
66	5.1	Physics beyond the Stnadard Model	50
67	5.2	Higgs Production Mechanisms	50
68	5.3	Branching Ratios	50

69	5.4	Discovery	50
70	5.5	Fermion Decay Modes	50
71	5.6	Boosted Higgs	50
72	III	The HbbISR Analysis	51
73	6	Data and Simulation Preparation	52
74	6.1	Data Used	52
75	6.2	Monte Carlo Samples	52
76	7	Physics Object Selection	53
77	7.1	Calorimeter Jets	54
78	7.2	Track Jets	54
79	7.3	Fat Jets	54
80	7.4	B-tagged Jets	54
81	7.5	Muons	54
82	7.6	Overlap Removal	54
83	8	Event Selection	55
84	8.1	Selected Triggers	55
85	8.2	Pre-selection Studies	55
86	8.3	Signal Selection	55
87	8.4	Optimisation	55
88	9	Background Estimation	56
89	9.1	Multi-jet QCD estimation	56
90	9.2	$t\bar{t}$ control region	56
91	9.3	Single top estimation	56

92	9.4 Hadronic vector boson channel	56
93	10 Systematic Uncertainties	57
94	10.1 Theoretical Uncertainties	57
95	10.2 Experimental Uncertainties	57
96	11 Statistical Fit	58
97	11.1 Profile Likelihood Function	58
98	11.2 Fit Configuration	58
99	11.3 Statistical Tests	58
100	12 Results	59
101	12.1 Expectations	59
102	12.2 Statistical Analysis Results	59
103	12.3 Measurements and Limits	59
104	IV Conclusion	60
105	13 Conclusion	61
106	Bibliography	61
107	A Hadronic Vqq Sherpa Studies	64

108 List of Figures

109	2.1	Summary of several Standard Model total and fiducial production cross	
110		section measurements, corrected for leptonic branching fractions, com-	
111		pared to the corresponding theoretical expectations. All theoretical ex-	
112		pectations were calculated at NLO or higher. The dark-color error bar	
113		represents the statistical uncertainty. The lighter-color error bar repre-	
114		sents the full uncertainty, including systematics and luminosity uncer-	
115		tainties. The data/theory ratio, luminosity used and reference for each	
116		measurement are also shown. Uncertainties for the theoretical predictions	
117		are quoted from the original ATLAS papers. They were not always eval-	
118		uated using the same prescriptions for PDFs and scales. The Wgamma	
119		and Zgamma theoretical cross-sections have non-perturbative corrections	
120		applied to the NNLO fixed order calculations (PRD 87, 112003 (2013)).	
121		Not all measurements are statistically significant yet.	6
122	2.2	Table of all observed fundamental particles of the current Standard Model.	7
123	2.3	A lower dimensionality representation of the shape of the Higgs Potential.	
124		The central peak represents a $v = 0$ rotationally symmetric unstable	
125		state, while the trough represents the infinite choices of minima that can	
126		be selected upon the spontaneous breaking of symmetry.	15
127	3.1	CERN accelerator complex	22
128	3.2	Labeled diagram of all the experiments at the LHC indicating the counter	
129		circulating beams and points of interest along the circumference of the	
130		accelerator.	24
131	3.3	Depiction of a LHC dipole magnet 2-in-1 design labeling the major com-	
132		ponents	25

133	3.4	Luminosity is monitored as both a running total known as the Integrated	
134		Luminosity as depicted in (a) and as an instantaneous quantity as shown	
135		in (b)	28
136	3.5	Pileup for data taking periods 2015 - 2018	29
137	4.1	[3] Here we see a cut-away side view of the ATLAS detector with the	
138		major components labeled. Note that within each of these labeled com-	
139		ponents there may exist multiple different detector technologies. For scale	
140		two people in red are shown standing between the disk muon chambers	
141		on the left side of the figure.	31
142	4.2	This slice of the ATLAS detector depicts how different particles interact	
143		with each component of the detector it crosses. A dashed line indicates	
144		no interaction while a solid line indicates interaction. Electrons (yel-	
145		low/green) and charged hadrons (red) interact with the tracker and curve	
146		in the solenoid's magnetic field. Electrons and photons (yellow/green) are	
147		absorbed by the Electromagnetic calorimeter. All hadrons (red/yellow)	
148		are absorbed by the Hadronic calorimeter. The muons (orange) curve in	
149		both the solenoid and torroid magnetic fields before exiting the detector.	
150		Finally, the neutrinos (white) pass through the entire detector without	
151		interacting.	34
152	4.3	[4] A cartoon view of the the LHC from above showing the SPS, LHC	
153		and the four main experiments of the LHC: ATLAS, CMS, LHCb, and	
154		ALICE. The standard cartesian coordinate system is shown with its origin	
155		at the ATLAS interaction point, the positive x -axis towards the center	
156		of the LHC, the positive y -axis pointing upwards, and the positive z -axis	
157		pointing along the beamline towards the "A-side"	35
158	4.4	Modified from [4] this cartoon represents a selection of pseudorapidity	
159		(η) values overlaid with some cartesian coordinates (dashed black lines).	
160		The redlines are drawn for $\eta = \pm 0.5, 1.0, 3.0$	36
161	4.5	[5] Diagram of inner detector	37
162	4.6	[8] Schematic of the Inner Detector including eta lines. Each component	
163		shown is cylindrically symmetric leading to a multi-layered detector. . .	38
164	4.7	[3] A cutaway diagram of ATLAS's sampling calorimeters	41
165	4.8	[3] Sketch of LAr EMC barrel module where the lead and liquid argon	
166		layers are visible in an accordion like geometry. Looking from the fore-	
167		ground to the back there are 3 different types of cells visible.	43

168	4.9	[3] Schematic of a tile calorimeter module including a depiction of the con-	
169		nection between the scintillator tile to the photomultiplier via a wavelength-	
170		shifting fibre.	45
171	4.10	[3] A cut-away diagram of the ATLAS muon system and its many sub-	
172		detectors.	47

173 List of Tables

Abstract

An Inclusive Search for the decay of a Boosted Higgs boson in the $H \rightarrow b\bar{b}$

channel with the ATLAS detector

by

Jacob Martin Pasner

Abstract placeholder

180

Dedication

181

Dedication

182

Dedication

Acknowledgments

184 Chapter 1

185 Introduction

186 Every dissertation should have an introduction. You might not realize it, but the
187 introduction should introduce the concepts, backgrouand, and goals of the dissertation.

188

Part I

189

Theoretical Motivations and the

190

Standard Model

Chapter 2

The Standard Model and Beyond

The Standard Model (SM) of Particle Physics is humanities best "guess" at the force laws that describe the observed behavior of all particles in our universe. Its formulation is a collection of Quantum Field Theories (QFT) that describe the following interactions of elementary matter in Nature: the electromagnetic force, the weak nuclear force and the strong nuclear force. Gravity is noticeably absent as currently there is no viable quantum theory for observed gravitational effects. The Glashow-Salam-Weinberg (GSW) theory of Quantum Electrodynamics (QED) describes the electromagnetic and weak forces, while Quantum Chromodynamics (QCD) describes the strong force. These theories form the following symmetry group of the Standard Model.

$$\underbrace{\mathrm{SU}_C(3)}_{\mathrm{QCD}} \otimes \underbrace{\mathrm{SU}_L(2) \otimes \mathrm{U}_Y(1)}_{\mathrm{GSW}}. \quad (2.1)$$

202 The gauge principle states that the SM Lagrangian and its predictions must be invariant
203 under local transformations using an operator from any of these constituent groups.
204 Thus, any theory must only include transformations and terms that maintain the local
205 invariance of the complete Lagrangian. In particular, this requirement was violated
206 by any attempt to include an explicit mass term for the Gauge Bosons of QED and
207 for all fermions. Around 1960 a possible solution to this lack of mass was proposed
208 in the form of the spontaneous breaking of the ElectroWeak symmetry, now known as
209 the Higgs mechanism. In the following sections I will go into more detail about the
210 Lagrangian formalism of the Standard Model, QCD, QED and this recently verified
211 Higgs Mechanism.

212 **2.1 The Standard Model**

213 At the turn of the 20th century our understanding of the constituent matter of the uni-
214 verse was limited to what we could see with microscopes and imply from the observations
215 of light and electricity, giving us evidence for both the photon and the electron. In the
216 first half of the century we discovered the field of subatomic physics with Rutherford's
217 1911 gold foil scattering experiment, and Dirac successfully demonstrated the quantiza-
218 tion of the electromagnetic field, the first step towards a fully Gauge Invariant Quantum
219 Field Theory. In the second half we literally delved deeper, discovering that the nucleus
220 contained structure and extended our theories to include the the complex mechanics of
221 quarks and gluons. With the discovery of the Higgs in 2013 the Standard Model has

222 become an irrefutable framework as can be seen in the high level of agreement between
223 theory and experiment in figure 2.1.

224 The QCD and QED theories predict two classes of particles: fermions and bosons shown
225 in figure 2.2. These particles represent the quanta of the quantum fields of the Standard
226 Model and the mediators of the fundamental forces of Nature.

227 2.1.1 Bosons

228 These spin-1 particles are known as the vector gauge bosons and are the force carriers
229 of the SM. The most commonly known is the electromagnetic force's un-charged and
230 massless photon (γ) which interacts with all charged particles and is often referred to
231 as "light". The weak nuclear force is involved in nuclear interactions such as beta
232 decays and is carried by 3 bosons all of which have mass and couple to all fermions;
233 the W^\pm bosons, which mediate the charged weak nuclear interaction and allow for
234 flavor changing currents; and the Z boson which mediates the neutral weak nuclear
235 interaction. Finally we have 8 massless gluons which mediate the strong nuclear force
236 and only interact with fermions with a "color" charge such as the quarks contained
237 inside the nucleus. The only spin-0 boson, the Higgs Boson (h) is the key to generating
238 mass terms in the SM Lagrangian for the massive Gauge Bosons and for fermions. This
239 is done through the so called Higgs Mechanism and is discussed in more detail in section
240 2.4.

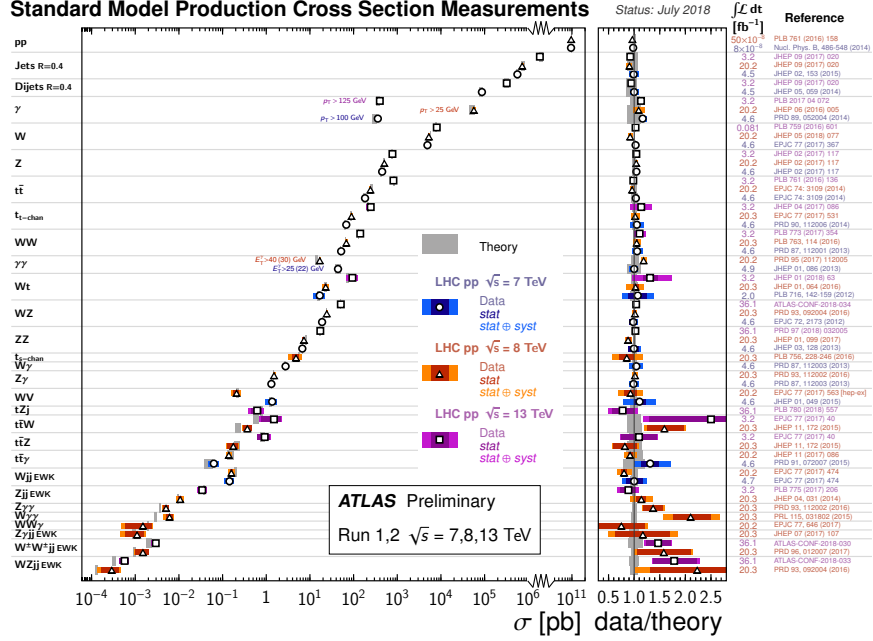


Figure 2.1: Summary of several Standard Model total and fiducial production cross section measurements, corrected for leptonic branching fractions, compared to the corresponding theoretical expectations. All theoretical expectations were calculated at NLO or higher. The dark-color error bar represents the statistical uncertainty. The lighter-color error bar represents the full uncertainty, including systematics and luminosity uncertainties. The data/theory ratio, luminosity used and reference for each measurement are also shown. Uncertainties for the theoretical predictions are quoted from the original ATLAS papers. They were not always evaluated using the same prescriptions for PDFs and scales. The $W\gamma$ and $Z\gamma$ theoretical cross-sections have non-perturbative corrections applied to the NNLO fixed order calculations (PRD 87, 112003 (2013)). Not all measurements are statistically significant yet.

Standard Model of Elementary Particles

three generations of matter (fermions)						interactions / force carriers (bosons)	
	I	II	III				
QUARKS	mass charge spin $\approx 2.2 \text{ MeV}/c^2$ $\frac{2}{3}$ $\frac{1}{2}$ u up	$\approx 1.28 \text{ GeV}/c^2$ $\frac{2}{3}$ $\frac{1}{2}$ c charm	$\approx 173.1 \text{ GeV}/c^2$ $\frac{2}{3}$ $\frac{1}{2}$ t top	$\approx 124.97 \text{ GeV}/c^2$ 0 0 1 g gluon			
	$\approx 4.7 \text{ MeV}/c^2$ $-\frac{1}{3}$ $\frac{1}{2}$ d down	$\approx 96 \text{ MeV}/c^2$ $-\frac{1}{3}$ $\frac{1}{2}$ s strange	$\approx 4.18 \text{ GeV}/c^2$ $-\frac{1}{3}$ $\frac{1}{2}$ b bottom	0 0 1 γ photon			
	$\approx 0.511 \text{ MeV}/c^2$ -1 $\frac{1}{2}$ e electron	$\approx 105.66 \text{ MeV}/c^2$ -1 $\frac{1}{2}$ μ muon	$\approx 1.7768 \text{ GeV}/c^2$ -1 $\frac{1}{2}$ τ tau	$\approx 91.19 \text{ GeV}/c^2$ 0 1 Z Z boson			
LEPTONS	$< 2.2 \text{ eV}/c^2$ 0 $\frac{1}{2}$ ν_e electron neutrino	$< 0.17 \text{ MeV}/c^2$ 0 $\frac{1}{2}$ ν_μ muon neutrino	$< 18.2 \text{ MeV}/c^2$ 0 $\frac{1}{2}$ ν_τ tau neutrino	$\approx 80.39 \text{ GeV}/c^2$ ± 1 1 W W boson			
					GAUGE BOSONS VECTOR BOSONS		
				SCALAR BOSONS			

Figure 2.2: Table of all observed fundamental particles of the current Standard Model.

241 2.1.2 Fermions

242 These spin-1/2 particles can be further broken up into two distinct families of particles,
243 the leptons and the quarks, both of which contain three "generations" each with an "up"
244 and "down" type particle. The leptons "up" type members are the electrically charged
245 electron (e), muon (μ) and tau (τ) while the "down" type are their electrically neutral
246 counterparts ν_e , ν_μ , ν_τ . The quarks "up" type members are the up (u), charm (c),
247 and top (t) each with a $+2/3$ elementary charge, while the "down" type members are
248 the down (d), strange (s), and bottom (b) all of which have a $-1/3$ elementary charge.
249 Each quark carries a "color" charge thus allowing them to participate in strong force
250 interactions. Due to the observed color confinement of the strong force these quarks are
251 only observed in colorless bound states known as "mesons" (1 quark and 1 anti-quark)
252 and "baryons" (an odd number of quarks and anti-quarks). All of the above fermions
253 have an anti-particle partner which has the opposite electrical charge but is otherwise
254 identical.

255 2.2 Quantum Electrodynamics

256 In the SM the Electromagnetic and Weak nuclear forces are unified into the Electroweak
257 interaction which is represented by the $SU(2)_L \times U(1)_Y$ gauge group. The L represents
258 the physical observable that the Weak interaction, and thus the $SU(2)$ transformation,
259 only acts on left handed particle states. The Y states that this is the $U(1)$ symmetry

for the weak hypercharge Y instead of the electromagnetic charge. The particle states for these interactions are solutions to the Dirac equation and are represented as Dirac spinor doublets (Ψ_L) for the left handed states, and as Dirac spinor singlets (Φ_R) for the right handed states. Thus when a general transformation from the Electroweak gauge group is applied to the left handed spinor doublet you get equation 2.2

$$\Psi_L \rightarrow \Psi'_L = \exp \left(\underbrace{ig' \frac{Y_L}{2} \zeta(x)}_{U(1)_Y} + \underbrace{ig_W \boldsymbol{\alpha}(x) \cdot \mathbf{T}}_{SU(2)_L} \right) \Psi_L. \quad (2.2)$$

For the right handed spinor singlet the $SU(2)_L$ doesn't contribute and you get equation 2.3

$$\Phi_R \rightarrow \Phi'_R = \exp \left(\underbrace{ig' \frac{Y_R}{2} \zeta(x)}_{U(1)_Y} \right) \Phi_R. \quad (2.3)$$

We can see that these local gauge transformations have introduced space-time dependent terms $\boldsymbol{\alpha}(x)$ and $\zeta(x)$ into our electroweak Lagrangian. Due to the derivatives contained within the kinetic term of this lagrangian, this new configuration would introduce additional terms, thus violating our required local gauge invariance. Luckily, we can remove these additional terms by replacing the standard derivative (∂_μ) with the covariant derivative (D_μ) as seen in equation 2.4 for the left handed states and 2.5 for

273 the right handed states.

$$D_\mu = \partial_\mu - \underbrace{\frac{1}{2}ig'B_\mu Y_L}_{U(1)_Y} - \underbrace{\frac{1}{2}ig_W \mathbf{W}_\mu \cdot \boldsymbol{\tau}}_{SU(2)_L} \quad (2.4)$$

$$D_\mu = \partial_\mu - \underbrace{\frac{1}{2}ig'B_\mu Y_R}_{U(1)_Y} \quad (2.5)$$

274 Here we see two new gauge fields; B_μ the weak hypercharge field and \mathbf{W}_μ the charged
 275 weak field. The form of these fields is chosen such that the final Lagrangian is invariant
 276 under $SU(2)_L \times U(1)_Y$ transformations, and thus we have restored gauge invariance for
 277 the kinetic term of our electroweak Lagrangian! Inserting these new definitions into the
 278 Lagrangian for the spinor field Ψ which satisfies the free-particle Dirac equation we get

$$\mathcal{L} = i\bar{\Psi}_L \gamma^\mu \left(\partial_\mu - \frac{1}{2}ig'B_\mu Y_L - \frac{1}{2}ig_W \mathbf{W}_\mu \cdot \boldsymbol{\tau} \right) \Psi_L + i\bar{\Phi}_R \gamma^\mu \left(\partial_\mu - \frac{1}{2}ig'B_\mu Y_R \right) \Phi_R \quad (2.6)$$

279 Next we must construct the gauge field self interaction and mass terms

$$\mathcal{L} = -\frac{1}{4}\mathbf{F}_{\mu\nu}\mathbf{F}^{\mu\nu} - \frac{1}{4}B_{\mu\nu}B^{\mu\nu} + \frac{1}{2}M_W^2 \mathbf{W}_\mu \mathbf{W}^\mu + \frac{1}{2}M_B^2 B_\mu B^\mu \quad (2.7)$$

280 where the field tensors $\mathbf{F}^{\mu\nu}$ and $B^{\mu\nu}$ are defined to be

$$\mathbf{F}^{\mu\nu} = \partial^\mu \mathbf{W}^\nu - \partial^\nu \mathbf{W}^\mu + g \mathbf{W}^\mu \times \mathbf{W}^\nu \quad (2.8)$$

$$B^{\mu\nu} = \partial^\mu \mathbf{B}^\nu - \partial^\nu \mathbf{B}^\mu \quad (2.9)$$

281 The field tensor terms in equation 2.7 are invariant under our gauge transformations,
 282 but simply plugging in equation 2.4 or equation 2.5 into the mass terms shows that
 283 these terms violate gauge invariance thus implying $M_W = 0$ and $M_B = 0$ in direct
 284 contradiction of the observed masses of the weak gauge bosons. This issue arises again
 285 for fermion mass terms as illustrated below for the electron field (e) expanded in its chiral
 286 basis.

$$m\bar{e}e = m \begin{pmatrix} e_R^\dagger & e_L^\dagger \end{pmatrix} \begin{pmatrix} e_L \\ e_R \end{pmatrix} = m(e_R^\dagger e_L + e_L^\dagger e_R) \quad (2.10)$$

287 Remembering that the left and right handed spinors of the electroweak interaction trans-
 288 form differently we see that this mixture of right and left fields violates gauge invariance.
 289 This again forces us to conclude that $m = 0$ in contradiction to the observation that
 290 fermions do indeed have mass. As mentioned in section 2.1.1 the resolution to these
 291 mass mysteries lies in the Higgs mechanism discussed in section 2.4

292 2.3 Quantum Chromodynamics

293 Quantum Chromodynamics is the continuation of the mathematical framework estab-
 294 lished by Quantum Electrodynamics (section 2.2, this time for the strong force described
 295 by the $SU(3)_C$ gauge group where the C represents the "color" charge of QCD. This
 296 color charge doesn't imply actual visible color, but is useful as an analogy to the visible
 297 spectrum where a combination of red, green, and blue generates white. For QCD the
 298 combination of red, green, and blue color charges results in a colorless object. As men-
 299 tioned in section 2.1.2 the quarks will contain a color (anti-color) charge represented by
 300 a color triplet field which transforms under the general $SU(3)$ transformation as shown
 301 here

$$q = \begin{pmatrix} q_r \\ q_g \\ q_b \end{pmatrix} \rightarrow q' = \exp \left(ig_s \sum_{k=1}^8 \eta_k(x) \frac{\lambda_k}{2} \right) q \quad (2.11)$$

302 Here the λ_k are the generators for $SU(3)$, $\eta(x)_k$ is the space-time dependency for each
 303 generator, and g_s is the strong coupling constant. As with QED, the introduction of
 304 these space-time dependant terms introduces new terms into the kinematic portion of
 305 the lagrangian thus spoiling our gauge invariance. Again, we introduce a covariant

306 derivative to restore invariance

$$D_\mu = \partial_\mu - ig_s G_\mu^k \frac{\lambda_k}{2} \quad (2.12)$$

307 Here the G_μ^k are the new fields introduced for the 8 gluons. These new fields transform
 308 under $SU(3)$ as shown in equation 2.13

$$G_\mu^k \rightarrow G_\mu'^k = G_\mu^k + \partial_\mu \eta_k(x) + g_s f_{klm} \eta_l(x) G_\mu^m \quad (2.13)$$

309 Given these definitions we can construct the QCD Lagrangian (\mathcal{L}_{QCD}) as shown in
 310 equation 2.14 where the gluon field tensor $G_k^{\mu\nu}$ is the one defined in equation 2.15

$$\mathcal{L}_{QCD} = \bar{q}(i\gamma_\mu D^\mu - m_q)q - \frac{1}{4} G_k^{\mu\nu} G_{k\mu\nu} \quad (2.14)$$

$$G_k^{\mu\nu} = \partial^\mu G_k^\nu - \partial^\nu G_k^\mu + g_s f_{klm} G_l^\mu G_m^\nu \quad (2.15)$$

311 The strong force is peculiar in that we experimentally observe only colorless objects in
 312 the form of bound states of quarks known as hadrons. Qualitatively, when a bound
 313 state of quarks (meson or baryon) is given sufficeint energy to separate the strong force
 314 dramatically increases in strength. At the point where the objects would separate, and
 315 thus no longer be colorless, it becomes energetically favorable to produce a quark/anti-
 316 quark pair in a process known as hadronization. In other words, attempting to separate

317 a bound quark state into its colored constituents simply results in new colorless bound
 318 states. This requirement of colorless objects by the strong force is known as color
 319 confinement. For highly energetic strong interactions at hadron colliders the result is
 320 an expanding chain of hadronizing quarks and gluons and their decay products known
 321 as a jet.

322 **2.4 The Higgs Mechanism**

323 The Higgs Mechanism is the system by which particles attain mass through the spon-
 324 taneous breaking of the Higgs potential, thus causing all particles it interacts with to
 325 have mass.

326 **2.4.1 Electroweak Symmetry Breaking**

327 The Higgs field is expressed as a complex doublet, Φ , and thus has four components as
 328 shown in equation 2.16

$$\Phi(x) = \begin{pmatrix} \phi^+ \\ \phi^0 \end{pmatrix} = \frac{1}{\sqrt{2}} \begin{pmatrix} \phi_1(x) + i\phi_2(x) \\ \phi_3(x) + i\phi_4(x) \end{pmatrix} \quad (2.16)$$

329 The four components of this field each represent a degree of freedom which will be
 330 used to give the longitudinal polarizations of the gauge bosons W^\pm, Z and the mass of
 331 the Higgs Boson. The resulting lagrangian for the higgs includes a kinetic term (K) as

332 well as the Higgs potential (V) all of which are invariant under the Electroweak gauge
 333 symmetry $SU(2)_L \times U(1)_Y$

$$\mathcal{L}_{\text{Higgs}} = \underbrace{(D_\mu \Phi)^\dagger D^\mu \Phi}_{\text{K}} - \underbrace{(\mu^2 \Phi^\dagger \Phi + \lambda (\Phi^\dagger \Phi)^2)}_{\text{V}} \quad (2.17)$$

334 Here we constrain $\mu^2 < 0$ and $\lambda > 0$ such that the potential forms a stable minima. The
 335 shape of this potential is shown in figure 2.3 and is often referred to as the "Mexican-hat"
 336 or "Wine-bottle" potential.

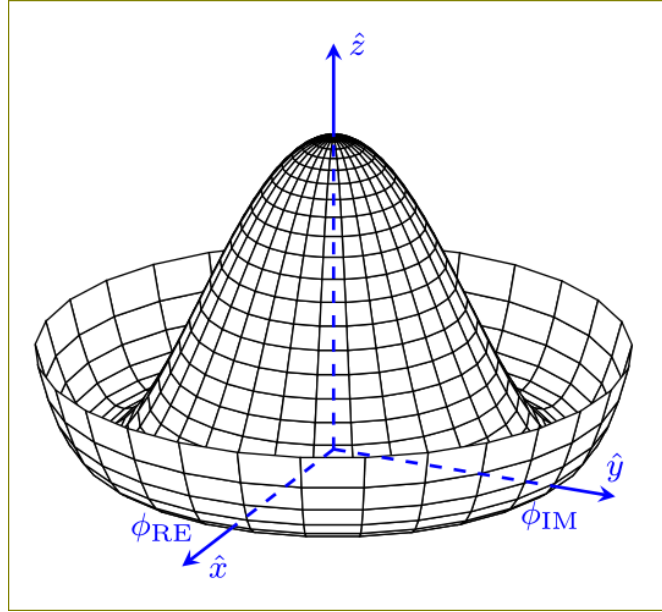


Figure 2.3: A lower dimensionality representation of the shape of the Higgs Potential. The central peak represents a $v = 0$ rotationally symmetric unstable state, while the trough represents the infinite choices of minima that can be selected upon the spontaneous breaking of symmetry.

337 Whatever you call it, this potential is significant in that its minimum is not at $\Phi = 0$
 338 but instead is symmetric around the origin thus defining an infinite number of states
 339 that minimize V . The value of this minima can be calculated by taking the derivative
 340 of V with respect to Φ and setting it equal to 0. This value, also known as the vacuum
 341 expectation value (vev) has been found to be $v \equiv \sqrt{\mu^2/\lambda} = 246$ GeV. In order to reach
 342 this ground state energy, the Higgs field must spontaneously break this symmetry, and
 343 thus acquire an arbitrary single value. For ease of calculation we orient our coordinate
 344 system such that

$$\langle \Phi(x) \rangle = \frac{1}{\sqrt{2}} \begin{pmatrix} 0 \\ v \end{pmatrix} \quad (2.18)$$

345 Next we parameterize small perturbations around the minimum of the Higgs potential
 346 as

$$\langle \Phi(x) \rangle = \frac{1}{\sqrt{2}} \begin{pmatrix} 0 \\ v + h(x) \end{pmatrix} \exp \left(i \frac{\tau^i}{2} \theta^i(x) \right) \quad (2.19)$$

347 Here the real scalar field $h(x)$ corresponds to radial perturbations of the minima and
 348 while the three $\theta^i(x)$ are the Nambu-Goldstone fields with values determined by your
 349 choice of gauge. Choosing the unitary gauge of $\theta^i(x) = 0$ and expanding the kinetic

350 term around the vev we get

$$\mathcal{L}_{\text{Higgs},K} = \frac{g^2 v^2}{8} \left((W_\mu^-)^\dagger W^{-\mu} + (W_\mu^+)^\dagger W^{+\mu} \right) + \frac{1}{2} \begin{pmatrix} W_\mu^{3\dagger} & B_\mu^\dagger \end{pmatrix} \mathbf{M}^2 \begin{pmatrix} W^{3\mu} \\ B^\mu \end{pmatrix} + \dots \quad (2.20)$$

351 Here the first term is the physical mass term for the W^\pm bosons where we have con-
 352 structed their charge eigenstates out of the $W^{1,2}$ fields like this $W^\pm = \frac{1}{\sqrt{2}}(W^1 \mp iW^2)$.
 353 The second term represents the mixture of the W^3 and B fields through the mass ma-
 354 trix \mathbf{M} . By diagonalizing this matrix and identifying the mass eigenstates we find the
 355 physical fields of the photon (γ) and the Z boson

$$\mathbf{M}_{\text{Diagonalized}}^2 = \begin{pmatrix} 0 & 0 \\ 0 & \frac{v^2}{4}(g^2 + g'^2) \end{pmatrix} \quad (2.21)$$

356 The upper left diagonal element corresponds to the massless photon while the lower
 357 right diagonal element gives the mass of the massive Z boson. This leaves us with the
 358 following masses for the 4 Electroweak bosons

$$m_W = \frac{1}{2}gv \quad , \quad m_Z = \frac{1}{2}v\sqrt{g^2 + g'^2} \quad , \quad m_\gamma = 0 \quad (2.22)$$

359 The masses of the W^\pm and Z gauge bosons can be related through the Weinberg angle

360 or mixing angle which

$$\theta_W = \cos^{-1} \left(\frac{g}{\sqrt{g^2 + g'^2}} \right) \rightarrow m_Z = \frac{m_W}{\cos \theta_W} \quad (2.23)$$

361 Using this definition we can write out the exact mixture of B and W^3 that make up the

362 photon and Z boson

$$\gamma = \cos(\theta_W)B + \sin(\theta_W)W^3 \quad (2.24)$$

$$Z = -\sin(\theta_W)B + \cos(\theta_W)W^3 \quad (2.25)$$

363 **2.4.2 Fermion Mass Terms**

364 **2.4.3 The Higgs Boson**

365

Part II

366

Experimental Apparatus and

367

Associated Facilities

368 Chapter 3

369 The Large Hadron Collider

370 Located 100 meters under the Swiss / French boarder lies the 26.7 kilometer Large
371 Hadron Collider (LHC) [1]. The culmination of a huge international collaboration,
372 this apparatus is used to produce proton and heavy ion collisions for observation by the
373 four major experiments at the LHC: ATLAS, CMS, LHCb, and ALICE. The system was
374 designed for a maximum center-of-mass energy of $\sqrt{s} = 14$ TeV and a peak instantaneous
375 luminosity of $L = 10^{34} \text{cm}^{-2} \text{s}^{-1}$.

376 The first LHC workshop was held in 1984 in Lausanne at the European Organization
377 for Nuclear Reserach (CERN) [2]. The nearly 30 year old case for a machine that
378 would push towards the discovery of the elusive Higgs Boson was presented using the
379 existing CERN accerlerator facilities and the Large Electron Positron (LEP) collider
380 tunnel. The proposal became reality on September 10, 2008 when the first proton beams
381 were circulated, only to have calamity strike 9 days later in the form of a catastrophic

382 electrical fault. The repairs and improvements lasted until November 2009 when the
383 LHC restarted. Since then this modern marvel has worked wonderfully and, as hoped,
384 lead to the discovery of the Higgs Boson by the CMS and ATLAS collaborations July
385 4, 2013.

386 The following chapter provides a brief introduction to the worlds most powerful accel-
387 erator starting with the little red bottle of hydrogen in building XXX, and ending with
388 the interaction point where protons collide at the highest energies ever produced.

389 **3.1 Particle Injecton Chain**

390 We begin with the most common element in the Universe, hydrogen, as our source of
391 protons. A bottle of hydrogen gas provides 100 microsecond pulses of raw H_2 which
392 is then injected into a Duoplasmatron. There, a strong electric field and free elctrons
393 from a cathode ionize the molecule into bare H^+ aka a proton! These protons are
394 then accelerated by a 90kV field, leaving the Duoplasmatron with 1.4% speed of light
395 ($\sim 4000\text{km/s}$) or, in relativistic units, about 83KeV. The bare protons are then fed
396 into the accelerating RadioFrequency (RF) cavities of Linear Accelerator 2 (LINAC2).
397 Inside, conductors charged by a powerful oscillating electromagnetic field accelerate the
398 protons resulting in a 50MeV energy. Along the way, small quadrupole magnets shape
399 the proton packet insuring they remain in a tight beam. This pattern of accleration
400 with RF cavities and shaping/turnig with magnets is then repeated with CERN's first

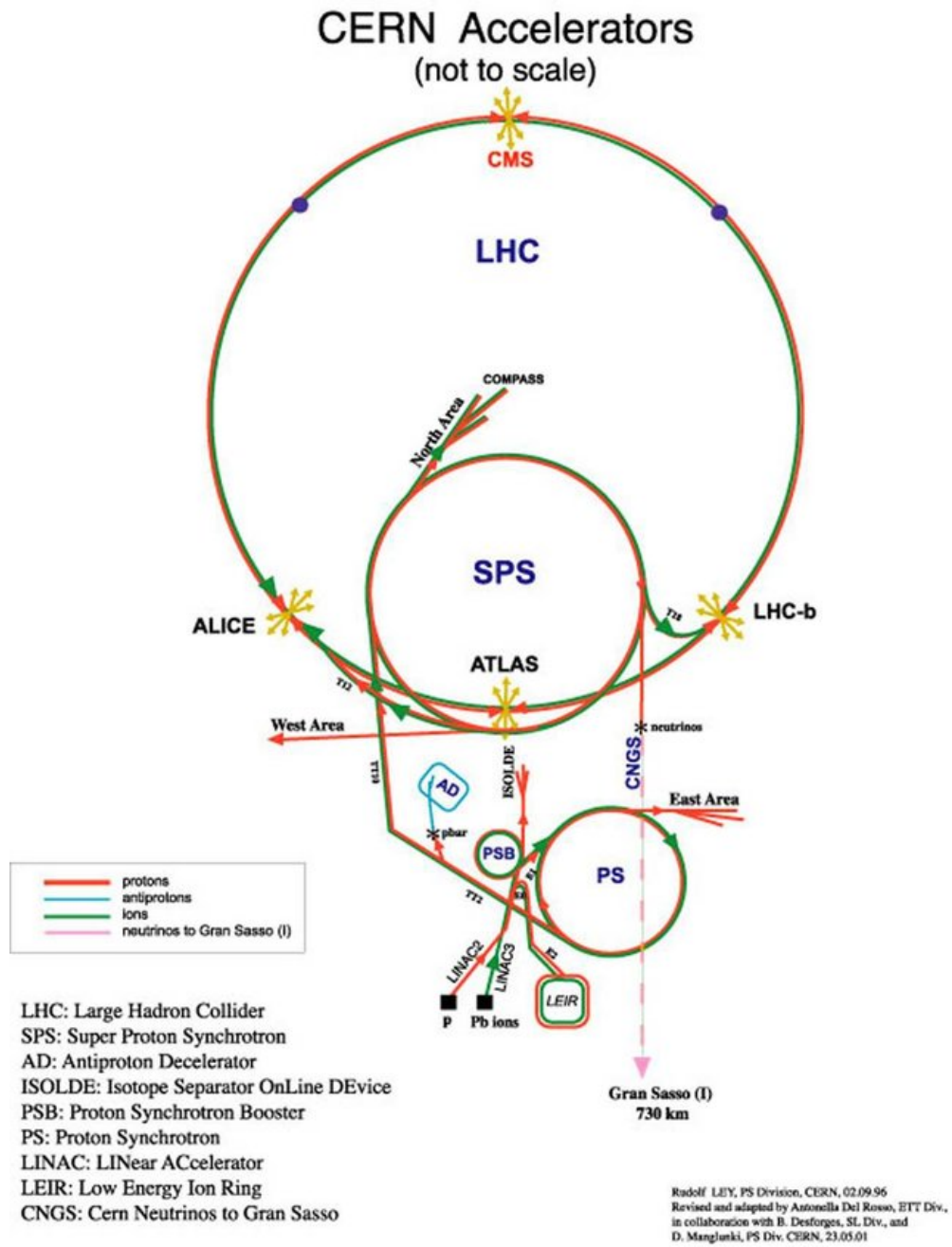


Figure 3.1: CERN accelerator complex

401 synchrotron, the Proton Synchrotron (PS) rendering a 1.4 GeV beam. The final step
402 before the LHC comes with the Super Proton Synchrotron where the same technologies
403 are implemented to produce 450 GeV protons, ready for injection into the LHC. A
404 diagrammatic representation of this chain can be seen in figure 3.1

405 In order to produce proton-proton collisions the LHC uses two beams circulating in
406 opposite directions. The beams are not continuous, but instead consist of bunches, or
407 buckets, of $\mathcal{O}(10^{11})$ protons with a spacing of 25ns. Given the LHC circumference this
408 allows for 3564 buckets, however only 2808 are filled per beam due to safety requirements
409 and injection limitations. Each beam takes 4 minutes and 20 seconds to fill and then an
410 additional 20 minutes to for the protons to reach their maximum energy of 7 TeV TeV,
411 or 99.99999991% the speed of light! Under normal operating conditions these beams
412 can be used for many hours.

413 **3.2 LHC layout and design**

414 While often depicted as a perfect circle the LHC is in reality an octagon with rounded
415 edges, called arcs, as can be seen in figure 3.2. Here you can see the counter circulating
416 beams of protons depicted in red and blue. These beams are focused and collided at
417 the 4 dedicated interaction points at rates of up to 40 MHz. Two of these points are
418 occupied by the ATLAS and CMS experiments, both of which are high luminosity,
419 multi-purposed experiments.

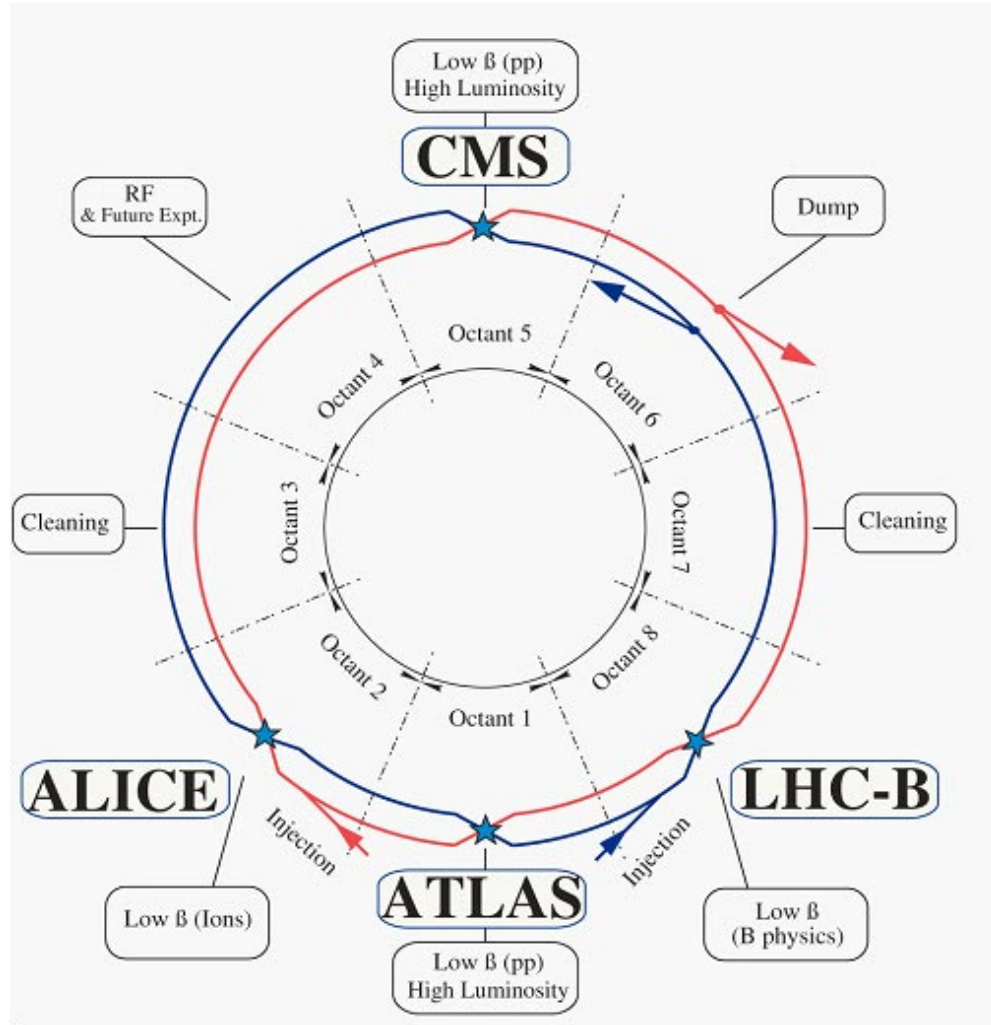


Figure 3.2: Labeled diagram of all the experiments at the LHC indicating the counter circulating beams and points of interest along the circumference of the accelerator.

420 The exact design of the tunnel is due to the experimental constraints of the original
 421 machine for which it was built, the Large Electron Positron (LEP) Collider. For the
 422 $\sim 2,000$ times lighter electron the maximum energy was limited by the synchrotron
 423 radiation, proportional to $\frac{1}{m^4}$, requiring long straight sections of accelerating RF cavities
 424 to recouperate the lost energy. Given that this effect is $\mathcal{O}(10^{13})$ times smaller for the
 425 proton the LHC is instead limited by our ability to design and construct magnets strong
 426 enough to bend the beam given the already determined curvature of the 8 arcs.

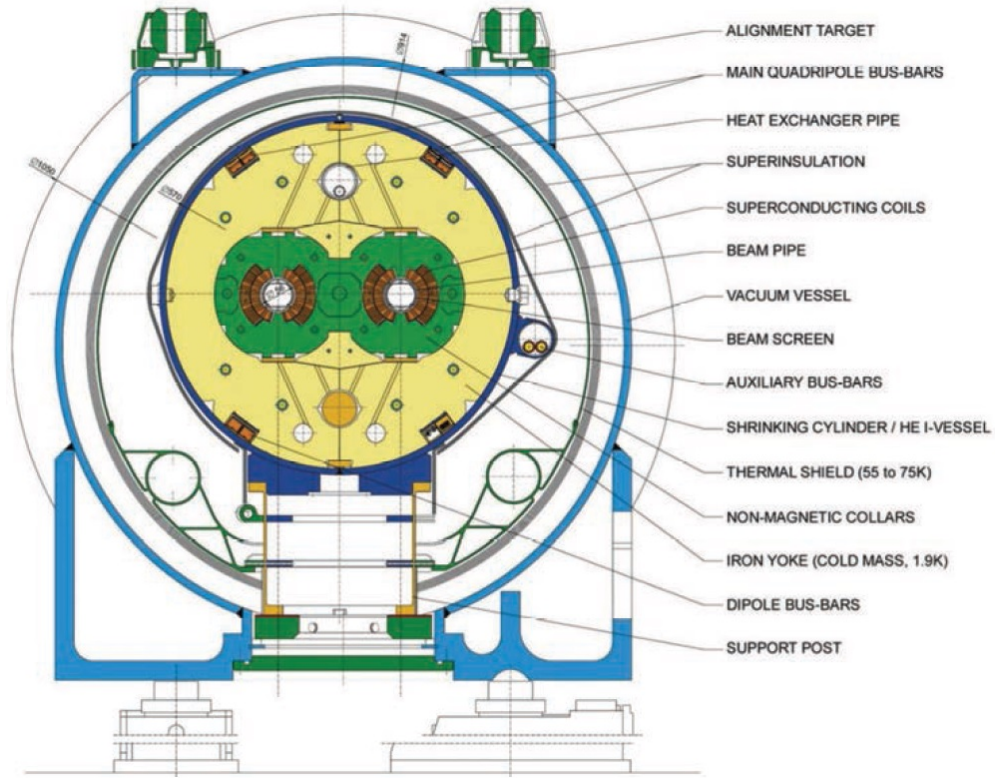


Figure 3.3: Depiction of a LHC dipole magnet 2-in-1 design labeling the major components

427 The oppositely circulating beams must each have their own ring and magnetic field
428 which lead to the creation of a twin-bore (i.e. "two-in-one") magnet design, a cross
429 section of which can be seen in figure 3.3. These magnets are constructed using NbTi
430 superconductors which are cooled to 2K using superfluid helium. These magnets are
431 designed to provide the needed 8.33 T magnetic field required to bend the beams at the
432 design beam energy of 7 TeV. In total 1231 of these 15 m long bending dipole magnets
433 are used, in association with 392 5-7m long quadrupole magnets which are responsible
434 for keeping the proton bunches in a tight beam by squeezing them either horizontally
435 or vertically.

436 **3.3 Performance**

437 Since the begining of its stable running in 2010 the LHC has performed well, even
438 exceeding our expectations. While the experiment itself is incredibly complex, the
439 performance of the machine, for the purposes of our analysis, can be reduced to two
440 numbers; the familiar center of mass energy of the beams and a less common quantity
441 known as the integrated luminosity.

442 For particle physics the integrated luminosity is proportional to the total number of
443 collisions recorded during a specified time period, while the instantaneous luminosity is
444 proportional to the bunch crossing rate along with the cross section of a proton-proton
445 interaction and represents the potential number of collisions per second. Knowing this

we can see that the integrated luminosity, L_{int} is simply the integral of the instantaneous luminosity $L_{inst.}$ for a choosen data period as seen in equation 3.1.

$$L_{int} = \int L_{inst.} dt \quad (3.1)$$

For a standard Gaussian beam, $L_{inst.}$ can be written as

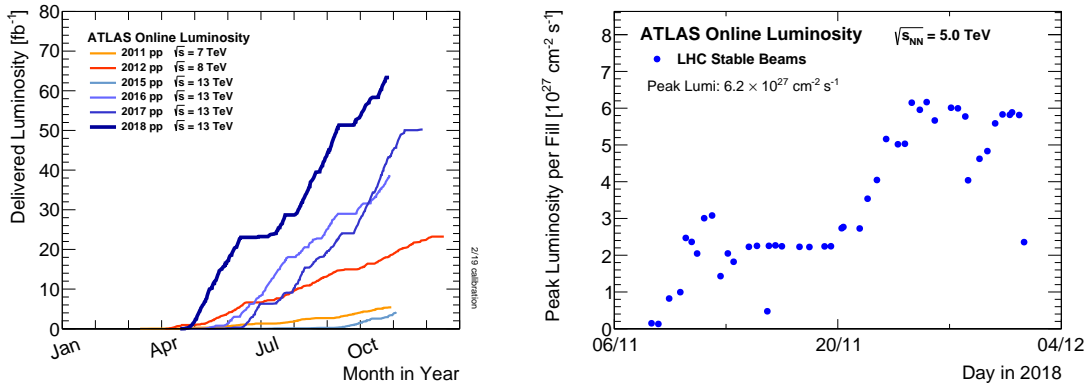
$$L = \frac{N_b^2 n_b f_{rev} \gamma_r}{4\pi \epsilon_n \beta^*} F \quad (3.2)$$

where N_b is the number of particles per bunch, n_b the number of bunches per beam, f_{rev} the revolution frequency, γ_r the relativistic gamma factor, ϵ_n the normalized transverse beam emittance, β^* the beta function at the collision point, and F the geometric luminosity reduction factor due to the crossing angle at the interaction point given by

$$F = \left(1 + \left(\frac{\theta_c \sigma_z}{2\sigma^*} \right)^2 \right)^{-1/2} \quad (3.3)$$

where θ_c is the full crossing angle at the interaction point, σ_z is the RMS bunch length, and σ^* is the transverse RMS beam size at the interaction point.

For the ATLAS experiment the integrated luminosity for each year can be seen in figure 3.4a as well as an example of the instantaneous luminosity for the choosen year in figure 3.4b.



(a) Integrated Luminosity 2011 - 2018 (b) 2018 Peak Instantaneous Luminosity

Figure 3.4: Luminosity is monitored as both a running total known as the Integrated Luminosity as depicted in (a) and as an instantaneous quantity as shown in (b)

3.4 Pile-up at the LHC

Given the large number of protons per bunch and the cross-section of a proton-proton interaction, the probability to observe multiple interactions per bunch crossing is quite high. These multiple-interaction are known as pile-up, μ or the time averaged representation $\langle\mu\rangle$, and come in two different forms:

1. **In-time pile-up:** These are the other proton-proton collisions that occur during the same bunch crossing as the primary interaction that caused the Data Acquisition (DAQ) system to trigger. These are the standard extra interactions we expect to observe as stated above.
2. **Out-of-time pile-up:** These are interactions that occur either before or after a

468 bunch crossing that causes the DAQ to trigger. This effect is generally due to the
 469 long integration times of some detector electronics.

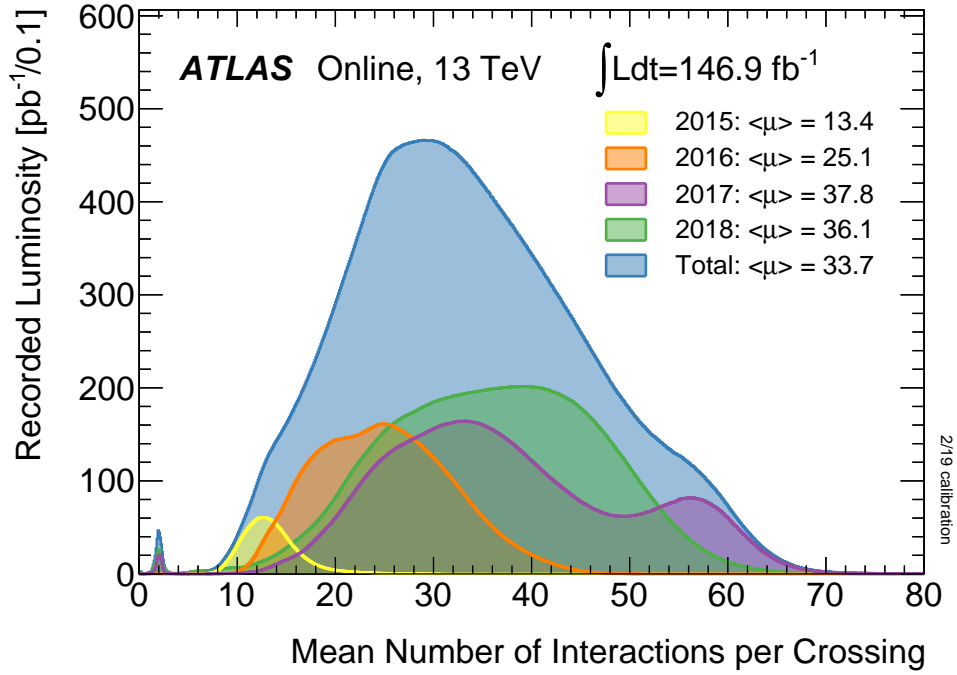


Figure 3.5: Pileup for data taking periods 2015 - 2018

470 The pile-up profile for past years can be seen in figure 3.5. The width of this distributino
 471 is due a combination of Poissonian statistics, the decrease in number of protons per bunch
 472 over the lifetime of a single run, and optimization tweaks to the beam's profile during
 473 runtime. Understanding and eliminating the noise from these pile-up events is crucial
 474 to reconstructing physics variables to represent the primary interaction we hope to
 475 observe.

476 Chapter 4

477 The ATLAS Detector

478 Given the immense energies available at the LHC, and the veritable zoo of particles we
479 are trying to detect, we require a general-purpose experiment in order to fully exploit
480 the full range of physics opportunities provided. Two international collaborations rose
481 to this challenge, the CMS (Compact Muon Solenoid) and ATLAS (A Torroidal LHC
482 Apparatus) experiments. While both have similar physics goals and each of them
483 strengths and weaknesses, this dissertation will focus on the ATLAS experiment and
484 the intricacies of its three main sub-detectors and two massive magnet systems depicted
485 in figure 4.1.

486 Originally proposed in 1994 the ATLAS experiment was completed in 2008. On July
487 4th, 2012 in a joint announcement the ATLAS and CMS experiments announced the
488 discovery of the long predicted Higgs Boson. The collaboration now boasts over 3000
489 physicists from 175 institutions spread across 38 countries and continues to probe

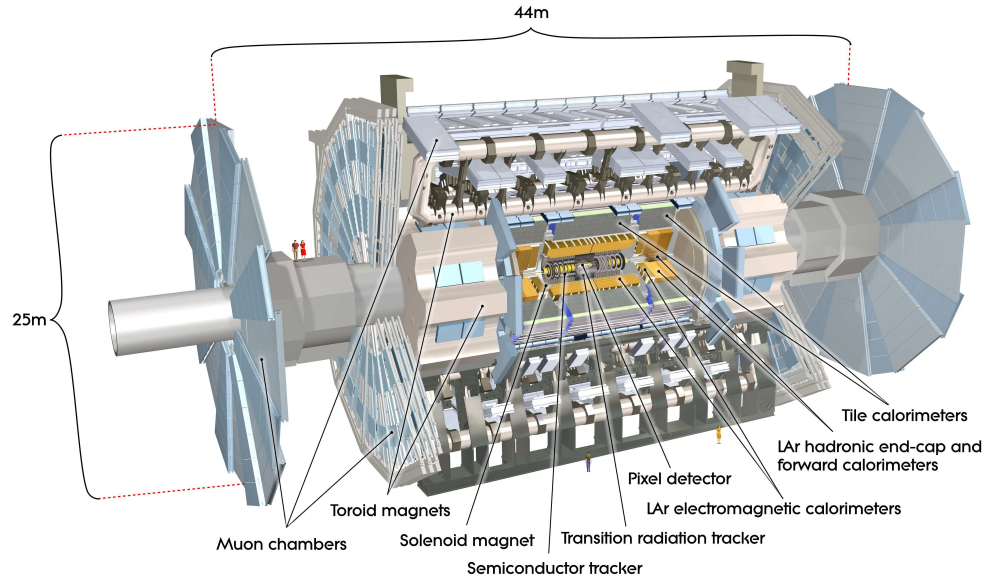


Figure 4.1: [3] Here we see a cut-away side view of the ATLAS detector with the major components labeled. Note that within each of these labeled components there may exist multiple different detector technologies. For scale two people in red are shown standing between the disk muon chambers on the left side of the figure.

490 the limits of the Standard Model in pursuit of answers to some of Humanities deepest
491 questions.

492 Located approximately 100 meters underground in a vast excavated chamber, the AT-
493 LAS detector rests its 7000 metric tonnes on a bed of concrete reinforced steel. Out of
494 it flows the signals of over 100 million electronic channels through a zip tied mass of
495 greater than 3000 kilometers of cabling. At its very center is one of the four interaction
496 points of the LHC, specifically Point 1, where the two counter circulating proton beams
497 are skillfully shaped and then collided by a series of magnets. The energetic particles
498 resultant from this collision then fly out in all directions into the bulk of the ATLAS
499 detector.

500 The first sub-system they meet is the Inner Detector (ID) and its many layers of strip
501 and pixel silicon detectors along with a transition radiation gaseous wire detector, all
502 bathed in the 2T magnetic field of the surrounding superconducting solenoidal magnet.
503 This system exploits the ionization of charged particles to track their curved trajectory
504 through the magnetic field. This curvature gives us charge information, a momentum
505 measurement, and precision 3D vertices crucial to the identification of the secondary
506 vertices of a b-hadron decay.

507 Outside of the solenoid the particles are faced with first the Electromagnetic and then
508 the Hadronic sampling calorimeters. Here, layers of scintillator and high radiation length
509 materials are implemented to measure the energy of electrons, photons, and hadrons.
510 As the goal is to completely absorb the energy of all outgoing particles the calorimeter

511 has a nearly 4π solid angle coverage.

512 Finally we have the muon system surrounding the calorimeter and equipped with its
513 own torroidal magnet system. Here the charged muon bends in the magnetic field
514 while leaving a trail of ionization in the muon spectrometer before exiting the detector
515 completely. Neutrinos are the only other standard model particle that leave the detector,
516 however they do so without detection. A depiction of the various particle interactions
517 with the different detector sub-systems can be seen in figure 4.2

518 In the following sections I will explain our choosen coordinate system and give a more
519 detailed reveiw of these 3 detector sub-systems.

520 4.1 ATLAS Coordinate System

521 Using the nominal interaction point as the origin, ATLAS uses a right handed coor-
522 dinate system where the positive x -axis points towards the center of the LHC ring,
523 the positive y -axis points upwards, and the positive z -axis is defined by the counter
524 clockwise circulating beam direction as viewed from above shown in figure 4.3 [3].

525 Using these coordinates we can define the physical momentum of the objects measured
526 as $\vec{p} = (p_T, p_z)$ with p_T being the momentum of the object in the transverse plane and
527 p_z the momentum along the beam axis. Given the cylindrical symmetry of ATLAS it
528 is desireable to define the polar angle θ from the beam axis with the $r - \phi$ plane being
529 perpendicular to that axis. Since the particles we observe are relativistically boosted

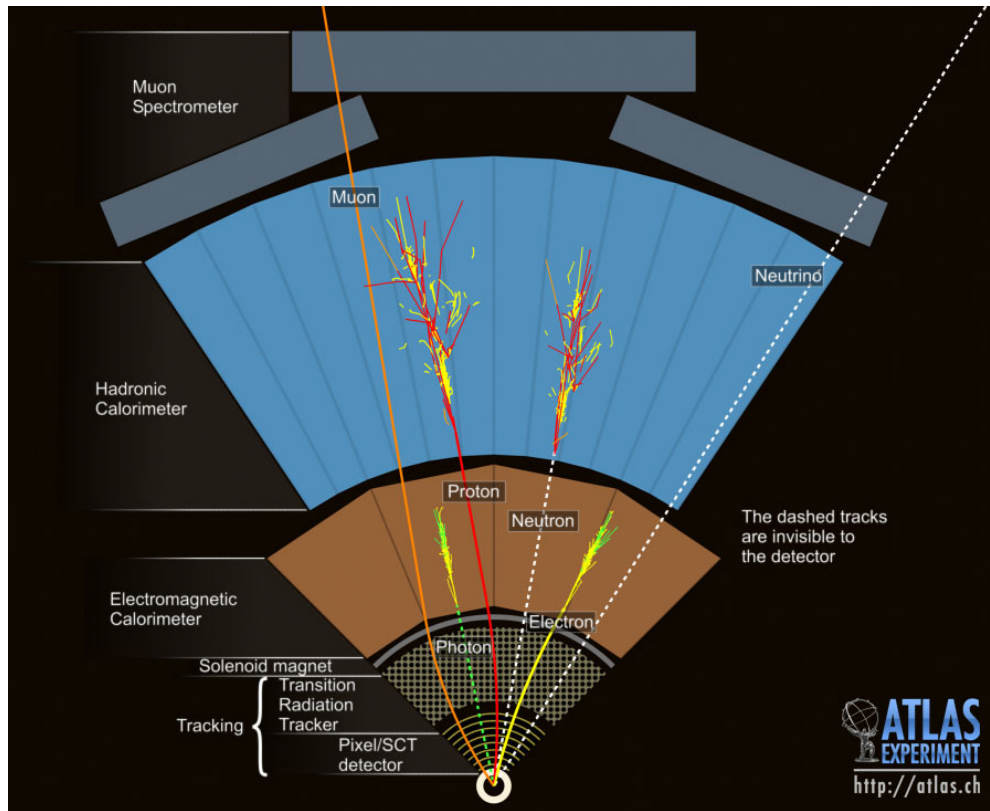


Figure 4.2: This slice of the ATLAS detector depicts how different particles interact with each component of the detector it crosses. A dashed line indicates no interaction while a solid line indicates interaction. Electrons (yellow/green) and charged hadrons (red) interact with the tracker and curve in the solenoid's magnetic field. Electrons and photons (yellow/green) are absorbed by the Electromagnetic calorimeter. All hadrons (red/yellow) are absorbed by the Hadronic calorimeter. The muons (orange) curve in both the solenoid and torroid magnetic fields before exiting the detector. Finally, the neutrinos (white) pass through the entire detector without interacting.

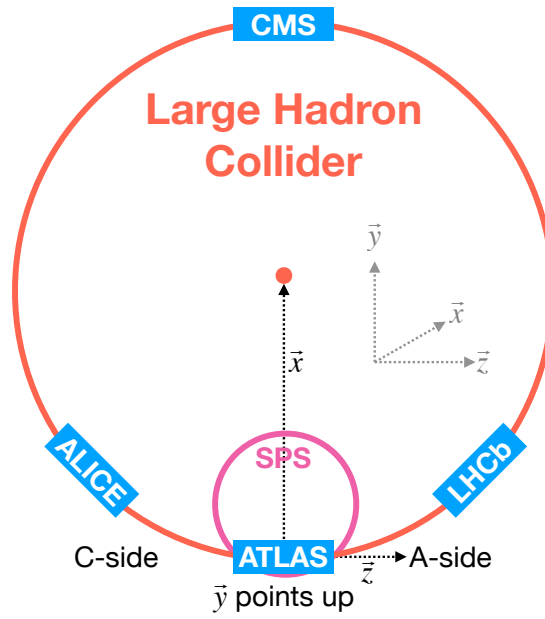


Figure 4.3: [4] A cartoon view of the the LHC from above showing the SPS, LHC and the four main experiments of the LHC: ATLAS, CMS, LHCb, and ALICE. The standard cartesian coordinate system is shown with its origin at the ATLAS interaction point, the positive x -axis towards the center of the LHC, the positive y -axis pointing upwards, and the positive z -axis pointing along the beamline towards the "A-side"

530 in the z -axis it is desirable to use the Lorentz invariant quantity pseudorapidity (η)
 531 defined in terms of the polar angle by

$$\eta = -\ln \tan \left(\frac{\theta}{2} \right). \quad (4.1)$$

532 where $\eta = 0$ is in the $x - y$ plane and larger values of $|\eta|$ being closer to the beam axis
 533 as can be seen in figure 4.4.

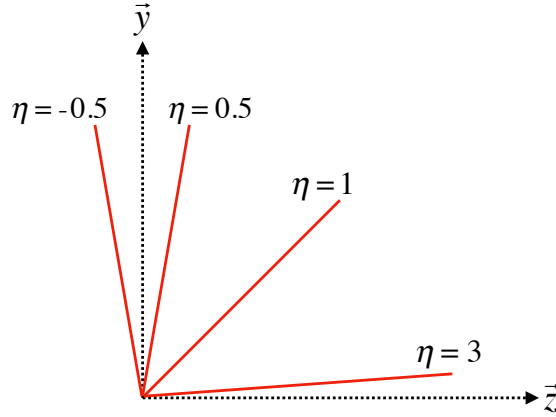


Figure 4.4: Modified from [4] this cartoon represents a selection of pseudorapidity (η) values overlaid with some cartesian coordinates (dashed black lines). The redlines are drawn for $\eta = \pm 0.5, 1.0, 3.0$

534 In this analysis the angular separation between objects in the detector is calculated and
 535 represented using the geometric quantity

$$\Delta R = \sqrt{(\Delta\eta)^2 + (\Delta\phi)^2} \quad (4.2)$$

4.2 Tracking with the Inner Detector

With its closest component, the insertable b-layer (IBL) [5], only 3.3 cm from the interaction point The Inner Detector (ID), shown in figure 4.5 [6, 7], faces the incredible challenge of providing precision momentum resolution and identification of both primary and secondary vertex measurements of charged tracks all while receiving the highest fluence.

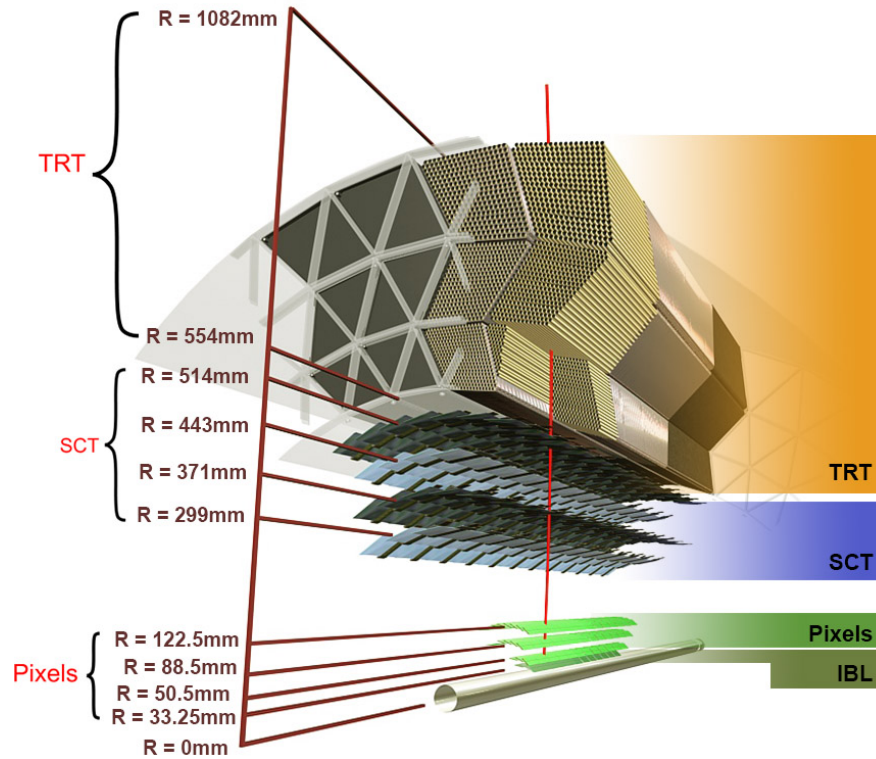


Figure 4.5: [5] Diagram of inner detector

It is designed to be very compact to reduce the probability of a particle decaying inside and to give precision measurements of the particles curvature in the 2T solenoidal

544 magnetic field. This leads to excellent momentum resolution above the nominal p_T
 545 threshold of 0.5GeV and within the pseudorapidity range of $|\eta| < 2.5$ as shown in figure
 546 4.6

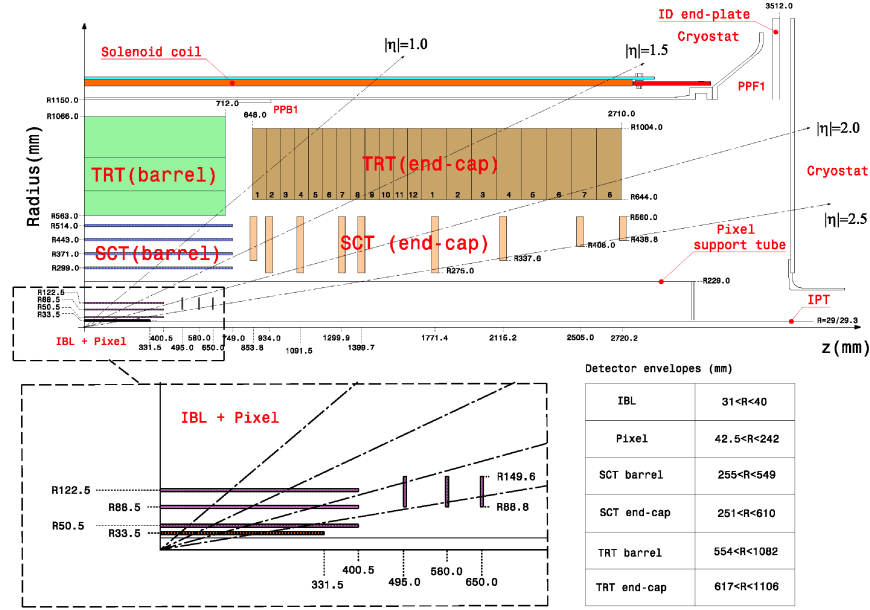


Figure 4.6: [8] Schematic of the Inner Detector including eta lines. Each component shown is cylindrically symmetric leading to a multi-layered detector.

547 The ID is composed of three different detector technologies for particle trajector re-
 548 construction: The Pixel Detector, Semiconductor Tracker (SCT) and the Transition
 549 Radiation Tracker (TRT). These will be discussed in the following sections.

550 4.2.1 Pixel Detector

551 The ATLAS Pixel Detector [3], the innermost subdetector of the ID, is designed to
552 give the best resolution possible as close as possible to the interaction point. This
553 is accomplished using the 4 barrel layers and the 3 disks per endcap as indicated in
554 figure 4.6. The inner most barrel layer, the IBL, has pixel dimensions of $50\mu\text{m}(\hat{\phi}) \times$
555 $250\mu\text{m}(\hat{z}) \times 200\mu\text{m}(\hat{r})$. For the other layers the dimensions are $50\mu\text{m}(\hat{\phi}) \times 400\mu\text{m}(\hat{z})$ for
556 about 90% of the pixels and $50\mu\text{m}(\hat{\phi}) \times 600\mu\text{m}(\hat{z})$ for the others, all with a thickness
557 of $250\mu\text{m}(\hat{r})$. This gives a total active area of 1.88m^2 collected through 92.4 million
558 readout channels, more than half of the total number of channels for ATLAS. This
559 detailed charged particle information very close to the interaction point is crucial not
560 only for pattern recognition for track reconstruction, but also for the reconstruction
561 of the primary and secondary vertices intrinsic to the decay of a b -hadrons, a critical
562 element of the analysis presented in this thesis.

563 4.2.2 Semiconductor Tracker

564 Encompassing the Pixel Detector, the Semiconductor Tracker (SCT) [3] is composed of
565 double sided silicon microstrips modules. Each side of the 4088 modules is constructed
566 out of two silicon strip sensors that are daisy chained together. The result is 768
567 composite strips each 12.6cm with an inter-strip pitch of $80\mu\text{m}$. In the barrel the strips
568 are aligned with the \hat{z} direction, while in the end caps they are aligned with the \hat{r}
569 direction. In both cases the separation of the strips is constant in $\hat{\phi}$. The two sides are

570 rotated with respect to each other by $40\mu\text{m}$ to allow for position measurement along the
 571 length of the strip. These modules are then used to tile the 4 barrel layers and 9 disks
 572 per endcap (18 disks in total) as seen in figure 4.6. This design is chosen to ensure
 573 that each charged track interacts with 8 strip layers (equivalent to four space points).
 574 This information is used to further measure the momentum and impact parameter, and
 575 as well as vertex identification of charged particles.

576 **4.2.3 Transition Radiation Tracker**

577 The Transition Radiation Tracker [3], the outermost subdetector of the ID, provides
 578 tracking through the detection of transition radiation from ultra-relativistic charged
 579 particles for $\eta < 2.0$ using 350,000 drift tube channels also known as straws. The
 580 4mm diameter straws are filled with a 70% Xe, 27% CO₂, and 3% O₂ gas mixture
 581 and a $31\mu\text{m}$ diameter gold-plated tungsten wire anode at the center for the collection
 582 of the ionization signal. In the barrel 73 azimuthally symmetric layers of 144cm straws
 583 are oriented parallel to the beam pipe with an electrical division in the center of each
 584 allowing the two sides to be read out separately. For each endcap the straws are radially
 585 oriented in 160 symmetric planes each containing 768 37cm long drift tubes shown
 586 in figure 4.6. In both the barrel and the end caps polypropylene fibers (barrel) or
 587 foils (encaps) function as the transition radiation material which causes the relativistic
 588 charged particles to radiate and thus ionize the gas in the straw. The amount of
 589 transition radiation produced is proportional to the Lorentz factor meaning that lighter

590 particles (e.g. electrons) will produce more radiation. Thus, by defining a high and low
 591 threshold, we can identify tracks belonging to electrons by requiring they register more
 592 high-threshold hits. There are typically 36 TRT hits per charged track.

593 4.3 Calorimetry

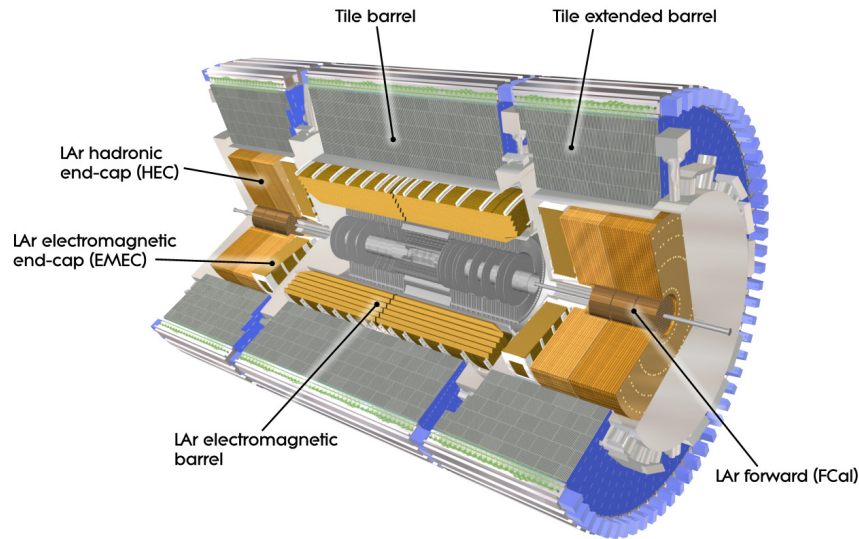


Figure 4.7: [3] A cutaway diagram of ATLAS's sampling calorimeters

594 Once the proton collision remnants have passed through the ID and it's surround-
 595 ing solenoid they enter into the ATLAS calorimeters depicted in figure 4.7. Sampling
 596 calorimeter technologies were choosen for their compact geometry and lower cost point.
 597 These are constructed by alternating layers of absorber, a dense material which reduces
 598 the incedent particles energy, and active material which produces a detectible signal
 599 when a partilce passes through. This means that the detected signal is only a fraction

600 of the total energy of the particle and thus requires a study of the calorimeter response
 601 for calibration purposes [9]. The first system, the Electromagnetic Calorimeter (EMC),
 602 is designed to measure the energy of electrons and photons which primarily lose their
 603 energy via bremsstrahlung and pair production electromagnetic interactions. Outside of
 604 the EMC is the Hadronic Calorimeter (HC) which is designed to measure the energy of
 605 jets of hadrons through their electromagnetic and strong interactions. These detectors
 606 cover the entire $|\eta| < 4.9$ range and provide complete containment of both Electromag-
 607 netic and Hadronic showers with higher granularity in the EMC for $|\eta| < 2.5$, the region
 608 matched to the ID, for precision measurements of electrons and photons. By instrument-
 609 ing this huge space in $|\eta|$ we can search for events with asymmetric energy deposits which
 610 imply the existence of a particle we didn't detect represented by missing transverse
 611 energy E_T^{miss} .

612 **4.3.1 Electromagnetic Calorimeter**

613 The innermost calorimeter, the Liquid Argon (LAr) Electromagnetic Calorimeter (EMC)
 614 [3], uses lead as the absorber and liquid argon as the active material in an "accordion
 615 geometry" as seen in figure 4.8. This geometry was chosen for uniform coverage in
 616 $\hat{\phi}$ due to its lack of un-instrumented cracks in the radial direction. The barrel region
 617 covers $|\eta| < 1.475$ and an end cap on each side covers $1.375 < |\eta| < 3.2$ each housed
 618 in their own cryostat. The barrel is composed of two half barrels with a 4mm gap at
 619 $z = 0$ and both end caps are divided into an inter wheel covering $2.5 < |\eta| < 3.2$ and

an outer wheel covering $1.375 < |\eta| < 2.5$.

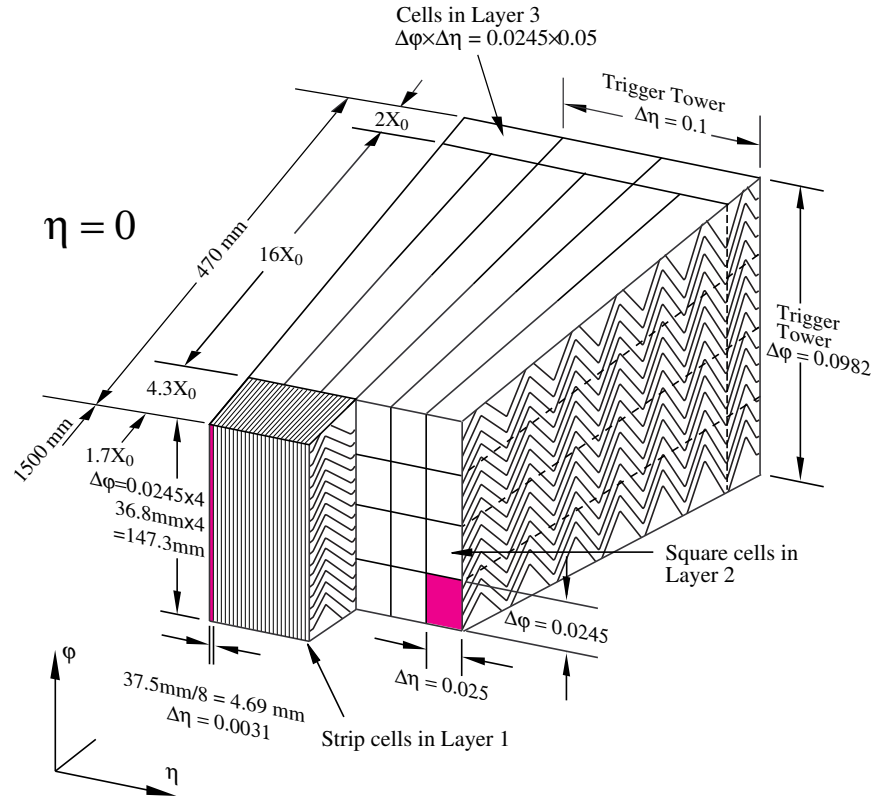


Figure 4.8: [3] Sketch of LAr EMC barrel module where the lead and liquid argon layers are visible in an accordion like geometry. Looking from the foreground to the back there are 3 different types of cells visible.

In the $|\eta| < 2.5$ region the EMC has 3 radial layers for precision physics measurements. Layer 1 consists of strip cells which are finely segmented with $\Delta\eta = 0.0031$ and $\Delta\phi = 0.0245$ allowing for precision position resolution which gives discrimination power between a single γ deposit and the π^0 characteristic $\gamma\gamma$ deposit. Layer 2, which collects the largest fraction of energy from electromagnetic shower, is segmented with

$\Delta\eta = .025$ and $\Delta\phi = 0.0245$. Layer 3 collects the tail of the electromagnetic shower using a coarser segmentation of $\Delta\eta = .05$ and $\Delta\phi = 0.0245$. Additionally, in the region $|\eta| < 1.8$ a thin pre-sampler, which contains no lead absorber, was placed in front of Layer 1 to allow for energy corrections due to losses upstream of the EMC. Combined the EMC is > 22 radiation lengths (X_0) in the barrel and $> 24 X_0$ in the end-caps, where a radiation length is the average distance an electron travels in a given material before losing $1/e$ of its original energy E_0 via bremsstrahlung radiation.

4.3.2 Hadronic Calorimeter

Directly outside the EMC envelope is the Hadronic Calorimeter (HC) system [3] which consists of three sampling calorimeter technologies: the Tile calorimeter, the LAr hadronic end-cap calorimeter (HEC) and the LAr forward calorimeter (FCal). Combined, these three subsystems give measurements of hadronic jet energies in the $0 < |\eta| < 4.9$ range. The tile calorimeter uses steel as the absorber layer and scintillating tiles as the active material and covers the region $|\eta| < 1.7$ with a barrel section flanked by two barrel extensions each divided azimuthally into 64 modules. These scintillator tiles are read out on two sides by wave-length shifting fibers connected to photomultiplier tubes as seen in figure 4.9. At $\eta = 0$ the total tile calorimeter thickness is 9.7 nuclear interaction lengths (λ), where λ is the average distance a hadron travels before interacting inelastically with a nucleus.

The HEC is composed of two independent wheels per end-cap located just past the

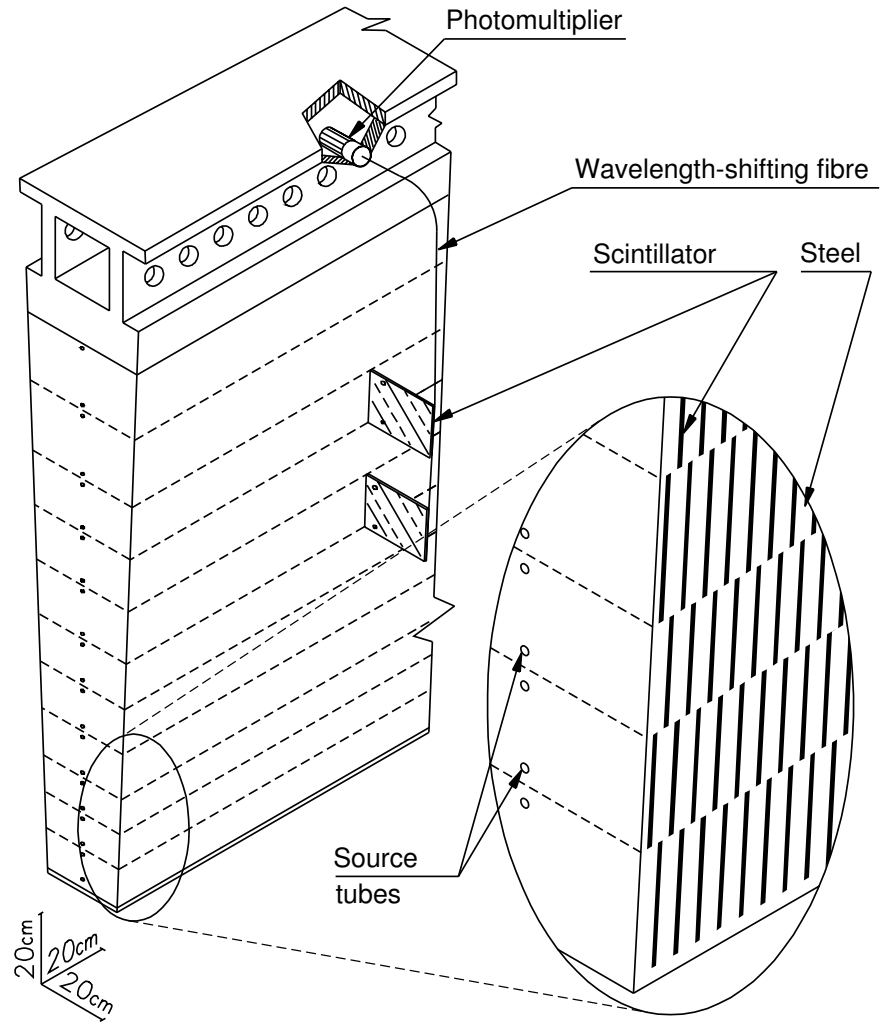


Figure 4.9: [3] Schematic of a tile calorimeter module including a depiction of the connection between the scintillator tile to the photomultiplier via a wavelength-shifting fibre.

646 EMC end-cap but sharing the same cryostat. This system uses copper as an absorber
 647 and liquid argon for the active material and covers the $1.5 < |\eta| < 3.2$ range using
 648 32 wdg-shaped modules per wheel. Finally, the FCal shares the same cryostat as the
 649 EMC and HEC end-caps and acts to extend the coverage of the combined calorimeter
 650 system to include the $3.1 < |\eta| < 4.9$ range. Each endcap contains 3 modules, the first
 651 an electromagnetic module (Copper/Liquid-Argon) which is followed by two hadronic
 652 modules which use (Tungsten/Liquid-Argon).

653 **4.4 Muon Spectrometer**

654 The ATLAS Muon Spectrometer (MS) [3], see figure 4.10, accomplishes tracking of
 655 charged particles in the $|\eta| < 2.7$ region for momentum reconstruction while also provid-
 656 ing triggering on charged particles in the $|\eta| < 2.4$ region. The magnetic field necessary
 657 for momentum reconstruction is provided by 3 air core torroid systems, one barrel tor-
 658 roid covering $|\eta| < 1.4$ and two endcap torroid systems which are inserted into the inner
 659 radius of the the barrel torroid to cover the $1.6 < |\eta| < 2.7$. The so called transition
 660 region $1.4 < |\eta| < 1.6$ between these two magnet systems is covered by a combination
 661 of the barrel and endcap torroid magnets. Similar to the ID the resolution is inversely
 662 proportional to the particle's incident momentum. Any muon with pT lower than 3GeV
 663 will never make it to the MS and thus will not be detected.

664 Precision tracking measurements for momentum reconstruction is accomplished using

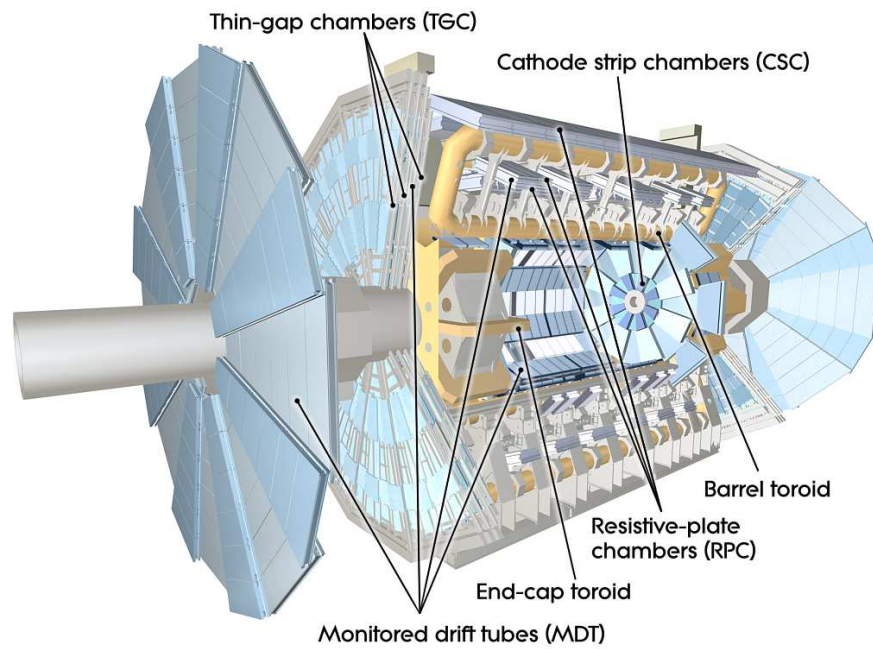


Figure 4.10: [3] A cut-away diagram of the ATLAS muon system and its many sub-detectors.

665 the Monitored Drift Tube chambers (MDTs) for $|\eta| < 2.0$ and using Cathode-Strip
666 Chambers (CSCs) for $2.0 < |\eta| < 2.7$. The MDT system consists of 1163 drift tube
667 chambers arranged in three to eight layers for varying η . The CSCs are designed to
668 withstand the higher rate and retain good time resolution using multiwire proportional
669 chambers with orthogonal segmented cathode planes.

670 The MS also gives nanosecond tracking information for triggering on muon tracks. This
671 is accomplished using Resistive Plate Chambers (RPC) in the barrel region $|\eta| < 1.05$
672 and Thin Gap Chambers (TGC) in the end-cap $1.05 < |\eta| < 2.4$ region. Both chamber
673 systems deliver a triggerable signal with a spread of 15–25 ns, thus providing the ability
674 to tag individual beam-crossings.

675 Chapter 5

676 Boosted Higgs at the LHC

677 Its July 4th, 2012 and the walls of building 500 are reverberating as Particle Physicists
678 around the world rejoice the discovery of the particle that gives all things mass, the
679 Higgs Boson.

680 **5.1 Physics beyond the Standard Model**

681 **5.2 Higgs Production Mechanisms**

682 **5.3 Branching Ratios**

683 **5.4 Discovery**

684 **5.5 Fermion Decay Modes**

685 **5.6 Boosted Higgs**

686

Part III

687

The HbbISR Analysis

688 Chapter 6

689 Data and Simulation Preparation

690 In order to compare data to theory ATLAS has developed an analysis chain which runs
691 both real data and simulated samples through the same processing, assuring a final
692 result which is as comparable as possible.

693 6.1 Data Used

694 6.2 Monte Carlo Samples

695 Chapter 7

696 Physics Object Selection

697 After the ATHENA Digitization step both data and monte carlo have the same format,
698 representing the three dimentional energy deposits. In order to analyze these deposits
699 they are cleaned, clustered and checked for overlap resulting in physics objects useful
700 for our specific analysis.

701 **7.1 Calorimeter Jets**

702 **7.2 Track Jets**

703 **7.3 Fat Jets**

704 **7.4 B-tagged Jets**

705 **7.5 Muons**

706 **7.6 Overlap Removal**

707 **Chapter 8**

708 **Event Selection**

709 Having created our physics objects we begin to make selections of what types of events
710 we want to consider given the goal of our analysis. In our boosted topology this means
711 considering things like momentum, jet collection efficiencies and background rejection.

712 **8.1 Selected Triggers**

713 **8.2 Pre-selection Studies**

714 **8.3 Signal Selection**

715 **8.4 Optimisation**

716 Chapter 9

717 Background Estimation

718 The dominant background was QCD. I worked on the $t\bar{t}$ control region. The V_{qq}
719 and single top backgrounds were estimated from monte carlo.

720 9.1 Multi-jet QCD estimation

721 9.2 $t\bar{t}$ control region

722 9.3 Single top estimation

723 9.4 Hadronic vector boson channel

724 **Chapter 10**

725 **Systematic Uncertainties**

726 **10.1 Theoretical Uncertainties**

727 **10.2 Experimental Uncertainties**

728 **Chapter 11**

729 **Statistical Fit**

730 The statistical fit in our analysis was accomplished using a framework developed for
731 Higgs searches.

732 **11.1 Profile Likelihood Function**

733 **11.2 Fit Configuration**

734 **11.3 Statistical Tests**

735 **Chapter 12**

736 **Results**

737 **12.1 Expectations**

738 **12.2 Statistical Analysis Results**

739 **12.3 Measurements and Limits**

740

Part IV

741

Conclusion

742 Chapter 13

743 Conclusion

744 I conclude that this section is the conclusion

Bibliography

- [1] Lyndon Evans and Philip Bryant. “LHC Machine”. In: *JINST* 3 (2008), S08001. DOI: 10.1088/1748-0221/3/08/S08001 (cit. on p. 20).
- [2] Chris Llewellyn Smith. “Genesis of the Large Hadron Collider”. In: *Phil. Trans. Roy. Soc. Lond.* A373.2032 (2014), p. 20140037. DOI: 10.1098/rsta.2014.0037 (cit. on p. 20).
- [3] ATLAS Collaboration. “The ATLAS Experiment at the CERN Large Hadron Collider”. In: *JINST* 3 (2008), S08003. DOI: 10.1088/1748-0221/3/08/S08003 (cit. on pp. 31, 33, 39–47).
- [4] Giordon Holtsberg Stark. “The search for supersymmetry in hadronic final states using boosted object reconstruction”. Presented 26 Apr 2018. May 2018. URL: <https://cds.cern.ch/record/2317296> (cit. on pp. 35, 36).
- [5] Karolos Potamianos. *The upgraded Pixel detector and the commissioning of the Inner Detector tracking of the ATLAS experiment for Run-2 at the Large Hadron Collider*. Tech. rep. ATL-PHYS-PROC-2016-104. 15 pages, EPS-HEP 2015 Proceed-

- 760 ings. Geneva: CERN, Aug. 2016. URL: <https://cds.cern.ch/record/2209070>
761 (cit. on p. 37).
- 762 [6] *ATLAS inner detector: Technical Design Report, 1*. Technical Design Report AT-
763 LAS. Geneva: CERN, 1997. URL: <http://cds.cern.ch/record/331063> (cit. on
764 p. 37).
- 765 [7] S Haywood et al. *ATLAS inner detector: Technical Design Report, 2*. Technical
766 Design Report ATLAS. Geneva: CERN, 1997. URL: [https://cds.cern.ch/](https://cds.cern.ch/record/331064)
767 [record/331064](https://cds.cern.ch/record/331064) (cit. on p. 37).
- 768 [8] B. Abbott et al. “Production and integration of the ATLAS Insertable B-Layer”.
769 In: *JINST* 13 (2018), T05008. DOI: 10.1088/1748-0221/13/05/T05008. arXiv:
770 1803.00844 [physics.ins-det] (cit. on p. 38).
- 771 [9] Christian Wolfgang Fabjan and F Gianotti. “Calorimetry for Particle Physics”.
772 In: *Rev. Mod. Phys.* 75.CERN-EP-2003-075 (Oct. 2003), 1243–1286. 96 p. DOI:
773 10.1103/RevModPhys.75.1243. URL: <https://cds.cern.ch/record/692252>
774 (cit. on p. 42).

⁷⁷⁵ **Appendix A**

⁷⁷⁶ **Hadronic Vqq Sherpa Studies**

⁷⁷⁷ Ancillary material should be put in appendices, which appear after the bibliography.